Article

Characterization of Tight Gas Sandstone Properties Based on Rock Physical Modeling and Seismic Inversion Methods

Han Jin, Cai Liu and Zhiqi Guo *

College of Geoexploration Science and Technology, Jilin University, Changchun 130021, China;
jinhan21@mails.jlu.edu.cn (H.J.); liucai@jlu.edu.cn (C.L.)
* Correspondence: guozhiqi@jlu.edu.cn

Abstract: Tight sandstones produce an increasing amount of natural gas worldwide. Apart from identifying the gas enrichment, the predictions of lithology and permeable zones are crucial for the prediction of tight gas sandstones. In the present study, a seismic inversion method is developed based on rock physical modeling, by which it is possible to directly predict the lithology and pore structure in tight formations. The double-porosity model is used as a modeling tool in considering complex pore structures. Based on the model, the microfracture porosity is then predicted using logging data, which are used as a factor to estimate microfractures. Parameters representing the lithology and pore structure are proposed and estimated using logging data analyses and rock physical modeling based on the framework of the Poisson impedance. Thereafter, a new AVO equation is established and extended to the form of an elastic impedance for a direct prediction of the lithology and pore structure parameters. Real data applications show that the indicators of lithology and permeable zones are consistent with the production status. They agree with the petrophysical properties measured in wellbores, thereby proving the applicability of the proposed method for the effective characterization of tight gas sandstones.

Keywords: lithology indicator; pore structure; rock physics model; seismic inversion; tight gas sandstone reservoir

1. Introduction

The evaluation of the Ordos Basin resource has shown that the total natural gas reserve in the basin is 15.16×10^{12} m^3, of which the tight gas reserve is approximately 10.37×10^{12} m^3. This accounts for about 68% of the total natural gas reserve and shows great potential for commercial gas production [1–3]. Tight gas is primarily formed in tight sandstones that are characterized by a porosity lower than 10% and permeability lower than 1 mD. The prediction of the lithology and gas enrichment and the detection of the pore structure in the interbedded strata composed of sandstones and mudstones are important for predicting favorable gas-bearing tight sandstones.

The prediction of gas saturation with seismic methods has been performed by many researchers [4–8]. Elastic and dispersion attributes that sre sensitive to gas saturation were then suggested for the identification of gas-bearing tight sandstones. In addition to the substantial porosity in the tight rocks, the development of fractures can provide spaces for gas storage and offer pathways for gas migration and accumulation. Therefore, the identification of pores and fractures by using seismic methods is highly important for a comprehensive characterization of tight gas sandstone reservoirs.

Azimuthal seismic inversion methods have usually been used to predict vertical structural fractures that have been developed from tectonic activities in tight formations [9–13]. The tight sandstones that are embedded with the vertical fractures are equivalent to horizontal transverse isotropy (HTI) media. However, core analyses have shown that microfractures with random orientations are the primary type of natural fractures in tight sandstones. In

this case, the azimuthal seismic inversion methods encounter difficulties in the detection of microfractures. Instead, appropriate rock physics methods should be used to quantify the elastic and seismic responses that are associated with microfractures. In practice, based on core and thin section analyses, various double-porosity (DP) models have been proposed to describe the poroelastic behaviors that are associated with complex pore structures in rocks [14–17]. In these structures, the total pore space is usually decomposed into round pores and microfractures of a low aspect ratio. The applicability of the DP model has been validated by experimental investigations [4,5] and numerical modeling based on well-log data [18]. Furthermore, various rock physics templates (RPTs) have been developed to estimate the pore structures in tight sandstones [19,20], as well as to identify fluids [21] and evaluate the brittleness [22]. However, the target-oriented features of the RPTs may limit the applicability of the methods in the evaluation of the petrophysical properties of the entire tight formation and within a range of depths.

It is advantageous to directly estimate the reservoir parameters (e.g., pore parameters) using seismic data [23–25]. Furthermore, petrophysical reservoir properties have also been evaluated by using seismic methods based on extended elastic impedance inversion [26], pre-stack elastic inversion [27], and quantitative interpretations [28,29]. By using seismic methods, despite the successful use of direct estimation of petrophysical properties, more rock physical constraints should be incorporated in the inversion based on well-log analyses and rock physical modeling. This should be done for improved characterization of tight sandstone gas reservoirs. In addition, the prediction of the lithology of a tight formation is an essential issue since the configuration of sand bodies basically controls the hydrocarbon distribution in the interbedded strata. At present, an accurate prediction of tight sandstones in the interbedded formations remains a challenge. This is due to the weak sensitivity of the seismic reflections in the target intervals.

The present study has focused on the development of a rock-physics-based seismic inversion method, by which it would be possible to directly predict the lithology and pore structure for improved characterization of tight gas sandstone reservoirs. At first, a method is proposed for the estimation of microfracture porosity in tight gas sandstones by using the DP model based on logging data. As the next step, parameters that represent the lithology and pore structure are proposed, which are based on well-log data analyses and rock physical estimations. Based on the obtained results, a new AVO equation is established and extended to an elastic impedance inversion for a direct prediction of lithology and pore structure parameters. Furthermore, the proposed methods are used for logging and seismic data that are obtained from the tight sandstone formations in Ordos Basin, China. The parameters of lithology and pore structures in tight formations could thereby be calculated. In addition, a combined parameter that considers the lithology, pore structure, and gas saturation is proposed for a comprehensive characterization of gas-bearing tight sandstones.

2. Methods

2.1. Estimation of the Microfracture Porosity of Tight Sandstones with the Rock Physics Model

The thin sections of the studied area show that tight sandstones can develop diverse types of pores (including intra-granular pores and dissolved inter-granular pores) and structural fractures (Figure 1). It is, therefore, necessary to establish a suitable rock physics model that can describe the elastic properties associated with pore structures in tight sandstones. In the present study, the total porosity (ϕ) was decomposed into round pores (ϕ_p) and microfractures (ϕ_f) (Figure 2a). The flowchart in Figure 2b illustrates the DP modeling method for tight sandstones. The elastic properties of the solid matrix were calculated by using the HSB theory [30], and the elastic moduli of the fluid-saturated tight sandstone were calculated by using the self-consistent approximation (SCA) approach [31]. The details of the rock physics method are illustrated in Appendix A.
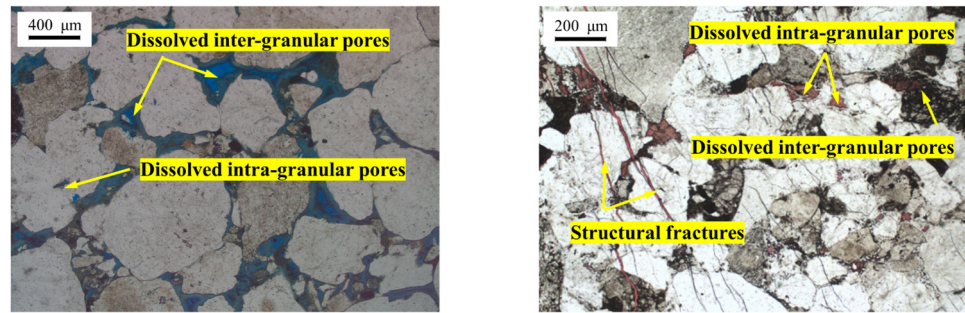
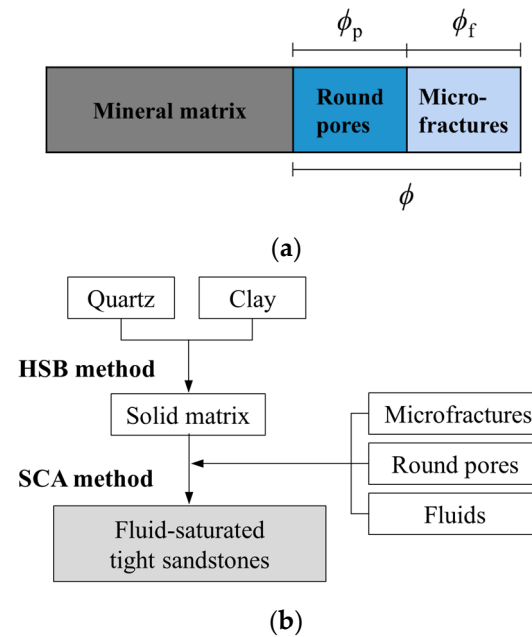**Figure 1.** Thin sections of the tight sandstones from the studied region.

(a)

(b)

Figure 2. (**a**) Schematic diagram and (**b**) modeling methods for the tight sandstones.

As can be seen in Figure 3, a flowchart was established for the prediction of ϕ_f from logging data using the DP model presented in Figure 2. For each sampling depth interval in the borehole, the porosity, mineralogical volumetric fractions, and fluids were used as input data in the calculations of P-wave velocities for a series of preset ϕ_f values. The value of ϕ_f that minimized the difference between the calculated ($V_{P\text{-calculated}}$) and measured ($V_{P\text{-measured}}$) P-wave velocity was denoted as the estimated ϕ_f value:

$$f\left(\phi_f\right) = min\left(\left|V_{P-\text{calculated}}\left(\phi_f\right) - V_{P-\text{measured}}\right|^2\right) \tag{1}$$

The corresponding S-wave velocity ($V_S(\phi_f)$) could also be obtained from the estimated ϕ_f value. By repeating this process for a range of depths in the borehole, the modeled $V_P(\phi_f)$ and $V_S(\phi_f)$, in addition to the estimated ϕ_f, could be generated.

2.2. Definition of Reservoir Parameters That Represent the Lithology and Pore Structure

Using the framework of the Poisson impedance [32], we proposed the lithology indicator (LI) and the factor of microfractures and pores (MP), respectively, for the evaluation of lithology and pore structure in tight sandstone formations:

$$\text{LI}(\theta_1) = I_P - I_S tan\theta_1 \tag{2}$$

$$\text{MP}(\theta_2) = I_P - I_S tan\theta_2 \tag{3}$$

where I_P denotes the P-wave impedance and I_S denotes the S-wave impedance. The angles θ_1 and θ_2 are the rotation angles that transfer the I_P and I_S values to LI and MP, respectively.
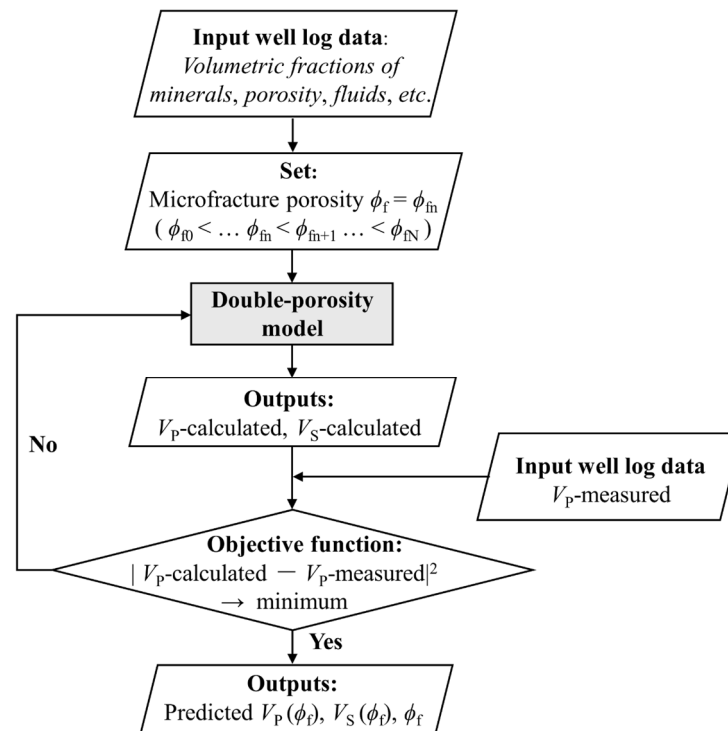

Figure 3. Flowchart for the estimation of microfracture porosity and velocities using the DP model and logging data.

As is further discussed in Section 3, the well-log analysis has indicated that the ratio of gamma-ray (GR) to the square of V_P ($GR/V_P{}^2$) can effectively identify tight sandstones in the studied tight formations. It can, therefore, be used to estimate the optimized θ_{max1} value in the determination of $LI(\theta_{max1})$ for lithology identification. In addition, the rock physical modeling has indicated that $\phi \times \phi_f$ can be used to evaluate the comprehensive effect of microfractures and pores. The factor $\phi \times \phi_f$ has, therefore, been used to estimate the optimized θ_{max2} value, which in turn has been used to obtain $MP(\theta_{max2})$ for the detection of permeable zones in tight formations.

2.3. A New AVO Equation for the Prediction of the Lithology and Pore Structure

$LI(\theta_{max1})$ and $MP(\theta_{max2})$ are, from here on, denoted as LI and MP, respectively. By using Equations (2) and (3) and the definitions $c_1 = \tan\theta_{max1}$ and $c_2 = \tan\theta_{max2}$, Equations (4) and (5) are obtained:

$$\frac{\Delta LI}{LI} = \frac{\Delta I_P - c_1 \Delta I_S}{I_P - c_1 I_S} = \frac{1}{1 - c_1 \frac{V_S}{V_P}} \left(\frac{\Delta I_P}{I_P} - c_1 \frac{V_S}{V_P} \frac{\Delta I_S}{I_S} \right) \tag{4}$$

$$\frac{\Delta MP}{MP} = \frac{\Delta I_P - c_2 \Delta I_S}{I_P - c_2 I_S} = \frac{1}{1 - c_2 \frac{V_S}{V_P}} \left(\frac{\Delta I_P}{I_P} - c_2 \frac{V_S}{V_P} \frac{\Delta I_S}{I_S} \right) \tag{5}$$

By using the following definitions (Equations (6) and (7)):

$$m_1 = 1 - c_1 \frac{V_S}{V_P}, \ n_1 = c_1 \frac{V_S}{V_P} \tag{6}$$

$$m_2 = 1 - c_2 \frac{V_S}{V_P}, \ n_2 = c_2 \frac{V_S}{V_P} \tag{7}$$

substituted into Equations (4) and (5), the following equations are formed (Equations (8) and (9)):

$$m_1 \frac{\Delta \text{LI}}{\text{LI}} = \frac{\Delta I_P}{I_P} - n_1 \frac{\Delta I_S}{I_S} \tag{8}$$

$$m_2 \frac{\Delta \text{MP}}{\text{MP}} = \frac{\Delta I_P}{I_P} - n_2 \frac{\Delta I_S}{I_S} \tag{9}$$

Equations (8) and (9) can be further reorganized, which results in Equations (10) and (11):

$$\frac{\Delta I_P}{I_P} = \frac{m_1 n_2}{n_2 - n_1} \frac{\Delta \text{LI}}{\text{LI}} - \frac{m_2 n_1}{n_2 - n_1} \frac{\Delta \text{MP}}{\text{MP}} \tag{10}$$

$$\frac{\Delta I_S}{I_S} = \frac{m_1}{n_2 - n_1} \frac{\Delta \text{LI}}{\text{LI}} - \frac{m_2}{n_2 - n_1} \frac{\Delta \text{MP}}{\text{MP}} \tag{11}$$

Furthermore, by substituting Equations (10) and (11) into the Fatti equation [33], i.e., Equation (12):

$$R_{\text{PP}}(\theta) = \frac{1}{2}(1 + tan^2\theta) \frac{\Delta I_P}{I_P} - 4\left(\frac{V_S}{V_P}\right)^2 sin^2\theta \frac{\Delta I_S}{I_S} \\ - \left(\frac{1}{2} tan^2\theta - 2\left(\frac{V_S}{V_P}\right)^2 sin^2\theta\right) \frac{\Delta \rho}{\rho} \tag{12}$$

Equation (13) is formed:

$$R_{\text{PP}}(\theta) = \frac{m_1}{n_2 - n_1}\left[\frac{n_2}{2}(1 + tan^2\theta) - 4\left(\frac{V_S}{V_P}\right)^2 sin^2\theta\right] \frac{\Delta \text{LI}}{\text{LI}} \\ - \frac{m_2}{n_2 - n_1}\left[\frac{n_1}{2}(1 + tan^2\theta) - 4\left(\frac{V_S}{V_P}\right)^2 sin^2\theta\right] \frac{\Delta \text{MP}}{\text{MP}} \\ - \left(\frac{1}{2} tan^2\theta - 2\left(\frac{V_S}{V_P}\right)^2 sin^2\theta\right) \frac{\Delta \rho}{\rho} \tag{13}$$

The new AVO equation (Equation (13)) provides the PP-wave reflection coefficient, $R_{\text{PP}}(\theta)$, which is represented by the density (ρ) and the parameters LI and MP.

2.4. Elastic Impedance Inversion Based on the New AVO Equation

According to the elastic impedance inversion method that was proposed by Connolly [34], the relationship between $R_{\text{PP}}(\theta)$ and the elastic impedance $\text{EI}(\theta)$ could be expressed as shown in Equation (14):

$$R_{\text{PP}}(\theta) = \frac{\text{EI}_2(\theta) - \text{EI}_1(\theta)}{\text{EI}_2(\theta) + \text{EI}_1(\theta)} = \frac{1}{2} \frac{\Delta \text{EI}(\theta)}{\text{EI}(\theta)} \approx \frac{1}{2}\Delta ln[\text{EI}(\theta)] \tag{14}$$

where $\text{EI}_1(\theta)$ and $\text{EI}_2(\theta)$ are the elastic impedances of the upper and lower media, respectively. Also, $\Delta \text{EI}(\theta)$ and EI denote the difference and average, respectively, of the elastic impedance across the interface.

By substituting Equation (13) into Equation (14) and by performing appropriate mathematical operations, Equation (15) is formed:

$$\text{EI}(\theta) = \text{LI}^{a(\theta)} \text{MP}^{b(\theta)} \rho^{c(\theta)} \tag{15}$$

where

$$a(\theta) = \frac{m_1}{n_2 - n_1}\left[n_2\left(1 + tan^2\theta\right) - 8\left(\frac{V_S}{V_P}\right)^2 sin^2\theta\right] \tag{16}$$

$$b(\theta) = -\frac{m_2}{n_2 - n_1}\left[n_1\left(1 + tan^2\theta\right) - 8\left(\frac{V_S}{V_P}\right)^2 sin^2\theta\right] \tag{17}$$

$$c(\theta) = 4\left(\frac{V_S}{V_P}\right)^2 sin^2\theta - tan^2\theta \tag{18}$$

A normalization operation is, thereafter, performed on Equation (15) according to the elastic impedance normalization method [35], which results in Equation (19):

$$EI(\theta) = EI_0 \left(\frac{LI}{LI_0}\right)^{a(\theta)} \left(\frac{MP}{MP_0}\right)^{b(\theta)} \left(\frac{\rho}{\rho_0}\right)^{c(\theta)} \tag{19}$$

where LI_0, MP_0, and ρ_0 represent the average values of the corresponding properties that have been obtained from the well-log data. Also, EI_0 indicates the elastic impedance normalization parameter with the expression shown in Equation (20):

$$EI_0 = LI_0^{(\frac{m_1 n_2}{n_2 - n_1})} MP_0^{(-\frac{m_2 n_1}{n_2 - n_1})} \tag{20}$$

After dividing both sides of Equation (19) by EI_0, and by taking the natural logarithm of each side, Equation (21) is formed:

$$ln\frac{EI(\theta)}{EI_0} = a(\theta)ln\left(\frac{LI}{LI_0}\right) + b(\theta)ln\left(\frac{MP}{MP_0}\right) + c(\theta)ln\left(\frac{\rho}{\rho_0}\right) \tag{21}$$

As can be seen in Equation (22), the inversion framework is finally established from Equation (21):

$$\begin{bmatrix} ln[EI(\theta_1)/EI_0] \\ ln[EI(\theta_2)/EI_0] \\ ln[EI(\theta_3)/EI_0] \end{bmatrix} = \begin{bmatrix} a(\theta_1) & b(\theta_1) & c(\theta_1) \\ a(\theta_2) & b(\theta_2) & c(\theta_2) \\ a(\theta_3) & b(\theta_3) & c(\theta_3) \end{bmatrix} \begin{bmatrix} ln(LI/LI_0) \\ ln(MP/MP_0) \\ ln(\rho/\rho_0) \end{bmatrix} \tag{22}$$

3. Results

3.1. Datasets

The study area in Figure 4 covers approximately 180 km^2 and the seismic survey was taken in 2018 in this area. Meanwhile, in this area, we collected data from five wells that were drilled and reached the tight gas sandstone reservoirs. As can be seen in Figure 4, the contour map of the seismic two-way travel time for the gas sandstone reservoir has a relatively simple tectonic structure. The locations of five wells (A–E) are indicated, out of which A and E are dry wells, and B, C, and D are gas-producing wells. Furthermore, Figure 5 presents the seismic section across the five wells, with illustrates GR logs from each borehole. The studied area was located in the Ordos Basin, China.
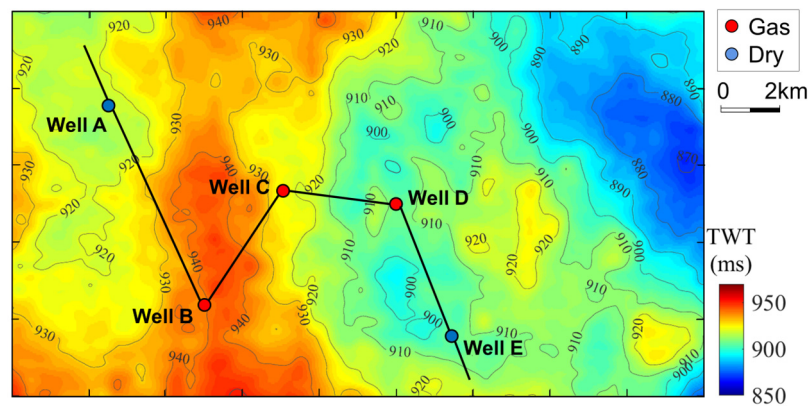

Figure 4. Two-way seismic travel time for the tight gas sandstone. The locations of the dry wells A and E are indicated by blue dots, and the locations of the gas wells B, C, and D are indicated by red dots.
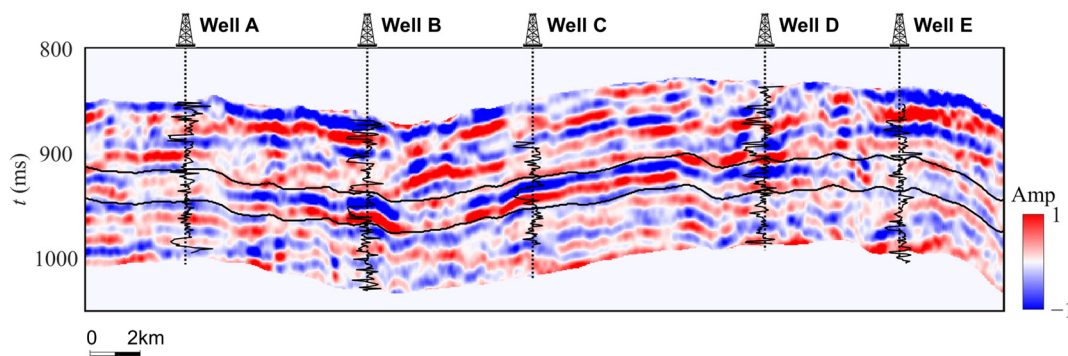
Figure 5. Profile across the wells A, B, C, D, and E, with overlapping GR loggings for the wellbores.

3.2. Prediction of the Microfracture Porosity by Using the DP Model

The values of the microfracture porosity, ϕ_f, for the tight gas sandstone reservoir in the studied area have been calculated by using the method presented in Figure 3. The logging data and predicted results for the A, B, and C wells are shown in Figure 6. The curves of ϕ_f were obtained by fitting the calculated values of V_P with the measured ones using Equation (1). As shown in Figure 6, the calculated V_P values fitted well with the corresponding experimental V_P values, which resulted in estimated ϕ_f values. In addition, the predicted V_S values agreed well with the corresponding V_S curves measured in wellbores, which validated the estimated ϕ_f results.

3.3. LI and MP Parameters That Are Represented by the Elastic Properties I_P and I_S

Figure 7 shows the logging curves of the elastic properties and reservoir parameters in the three wells A, B, and C. As discussed in Section 2.2, the GR/$V_P{}^2$ parameter showed improved performance in the identification of the tight sandstones, as compared with the GR parameter. The reason for this difference was that the tight sandstones became more separable from the mudstones when using GR/$V_P{}^2$. In addition, the $\phi \times \phi_f$ parameter could be used to estimate the comprehensive effects of the pore structures in the tight formations. Furthermore, the optimized LI(θ_{max1}) and MP(θ_{max2}) curves in Figure 7 were determined by using the estimated maximum correlation coefficients that are presented in Figure 8.

The method presented in Section 2.2 was used to estimate the correlation coefficients between the reservoir parameters (LI(θ_1) and MP(θ_2)) and the elastic impedances (I_P and I_S). As can be seen in Figure 8, the correlation coefficients for the three wells A, B, and C reached a maximum at approximately $\theta_{max1} = 80°$ for the optimized LI parameter (Equation (2)) and a maximum at approximately $\theta_{max2} = 45°$ for the optimized MP parameter (Equation (3)).

In the cross-plot of I_P versus LI (as color-coded by GR/$V_P{}^2$), it could be seen that the LI($\theta_{max1} = 80°$) parameter could effectively identify the lithology. The high values of LI($\theta_{max1} = 80°$) corresponded to low values of GR/$V_P{}^2$, indicating the lithology of the tight sandstone (Figure 9). In addition, the MP($\theta_{max1} = 45°$) parameter could effectively determine the pore structure that was identified by the $\phi \times \phi_f$ values, where low values of MP($\theta_{max1} = 45°$) corresponded to high $\phi \times \phi_f$ values (Figure 10). Thus, it has been shown that the MP($\theta_{max1} = 45°$) parameter can be used in the identification of permeable zones in tight formations.

3.4. Estimation of LI and MP by Using the Proposed Elastic Impedance Inversion Method

The LI($\theta_{max1} = 80°$) and MP($\theta_{max2} = 45°$) parameters were denoted as LI and MP. By using the elastic impedance inversion method presented in Section 2.4, the LI and MP parameters could be estimated directly by using the pre-stack seismic data. Furthermore, the EI values were computed from the pre-stack seismic data by using the inversion presented in Equation (22). These calculations were based on the method of Connolly [34], and the results were EI(5°), EI(15°), and EI(25°) (Figure 11).
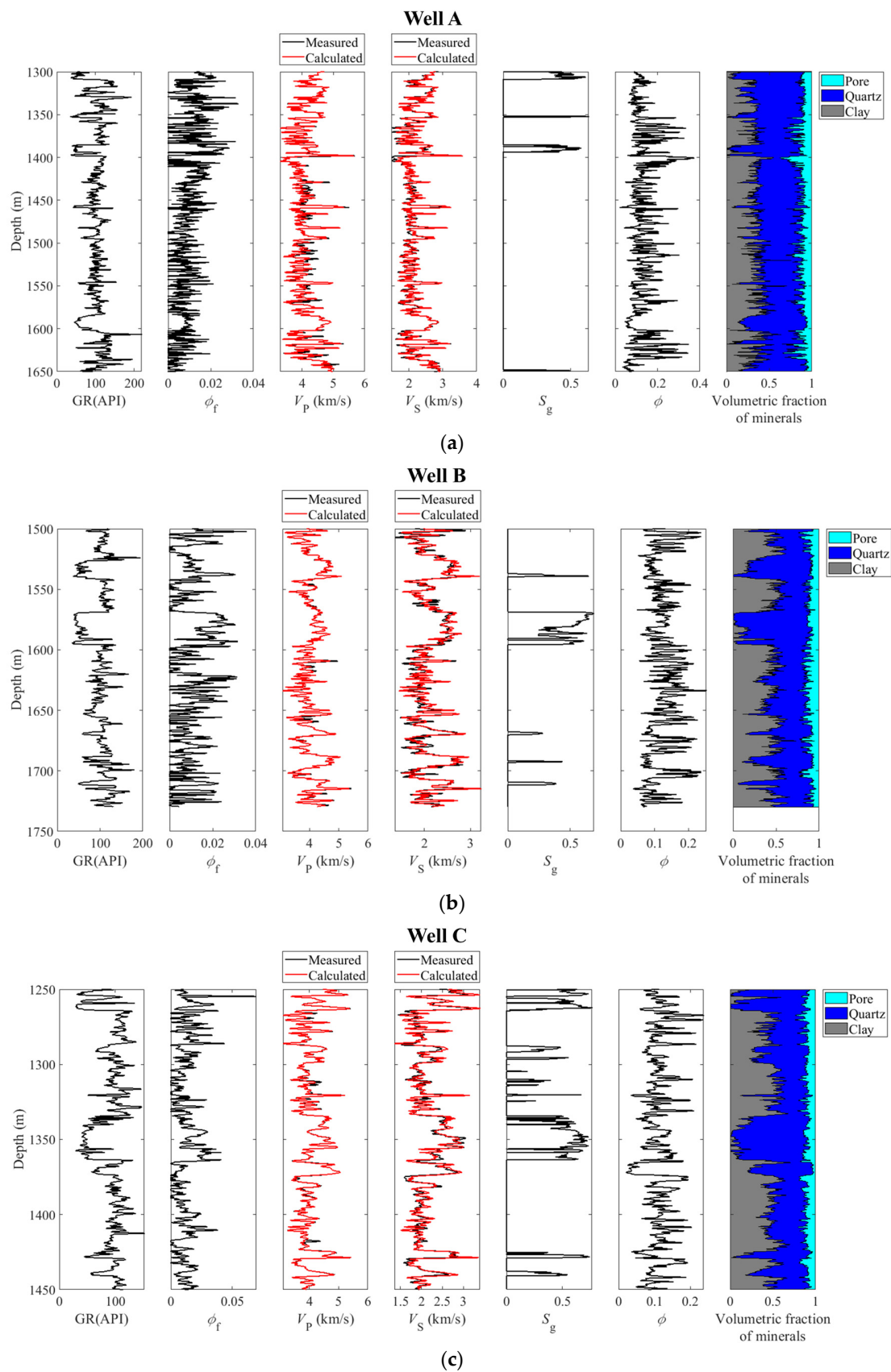
Well A

(**a**)

Well B

(**b**)

Well C

(**c**)

Figure 6. The curves of GR, ϕ_f, V_P, V_S, S_g, ϕ, and volumetric fractions of minerals for well (**a**) A, (**b**) B, and (**c**) C.
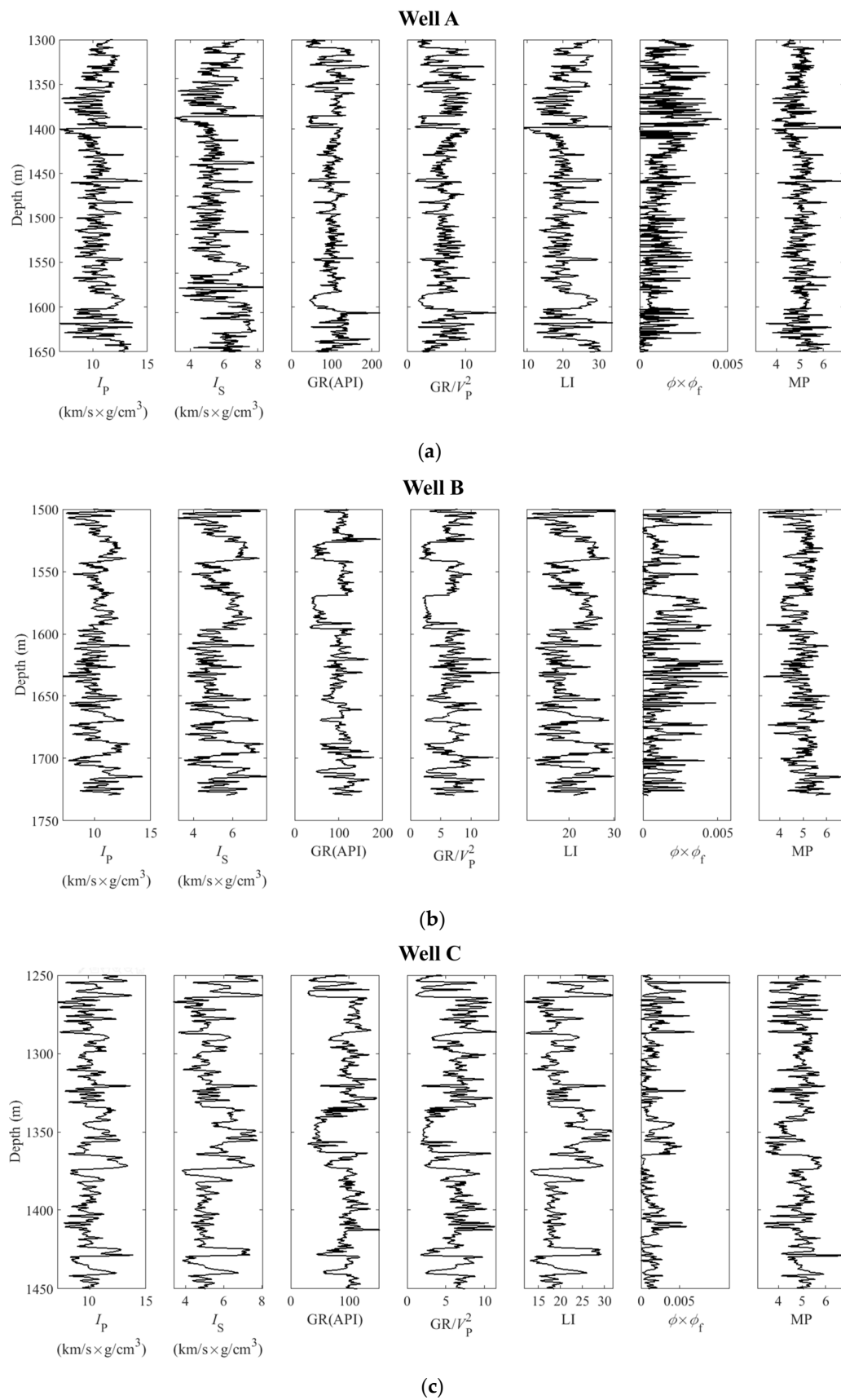
Figure 7. The curves of I_P, I_S, GR, GR/$V_P{}^2$, LI(θ_{max1} = 80°), $\phi \times \phi_f$, and MP(θ_{max2} = 45°) for well (**a**) A, (**b**) B, and (**c**) C.

(**a**)

(**b**)
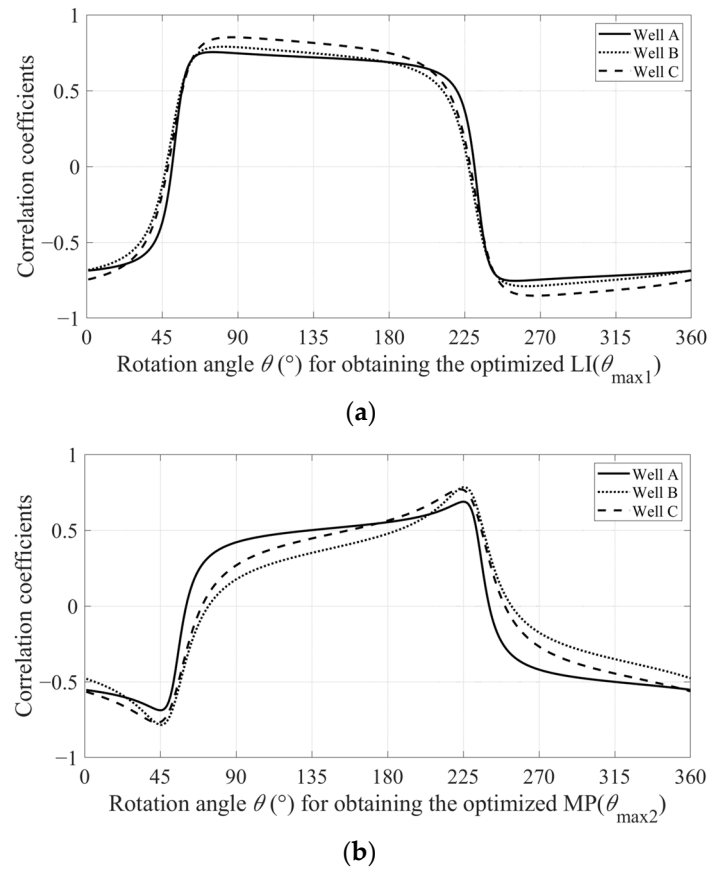
Figure 8. Correlation coefficients varying with rotation angles, θ, for obtaining (**a**) LI and (**b**) MP.
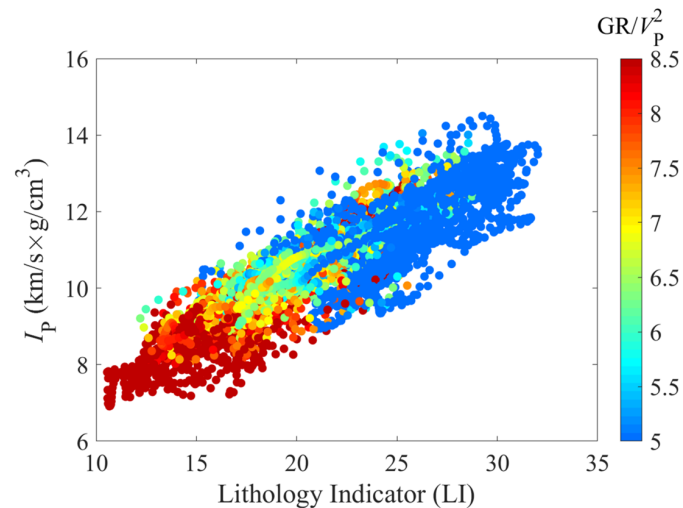

Figure 9. Cross-plot of I_P versus LI($\theta_{max1} = 80°$), as color-coded by GR/$V_P{}^2$.

Figure 12 shows the inverted LI profiles with overlapping GR logging curves. It was found that the tight sandstones, which were recognized by low GR values in the boreholes, could be well identified by the seismic-inverted LI parameter. Specifically, the tight sandstones in the gas-producing B and C wells corresponded to high-value anomalies of the LI parameter. In particular, the thin layers of tight sandstone in gas well D could be determined by the LI parameter with high accuracy. In addition, the LI parameter showed fewer anomalies in the dry wells A and E. The results presented in Figure 12 have validated the applicability of the LI parameter for the identification of tight sandstones that exhibit an optimal lithology for gas production.
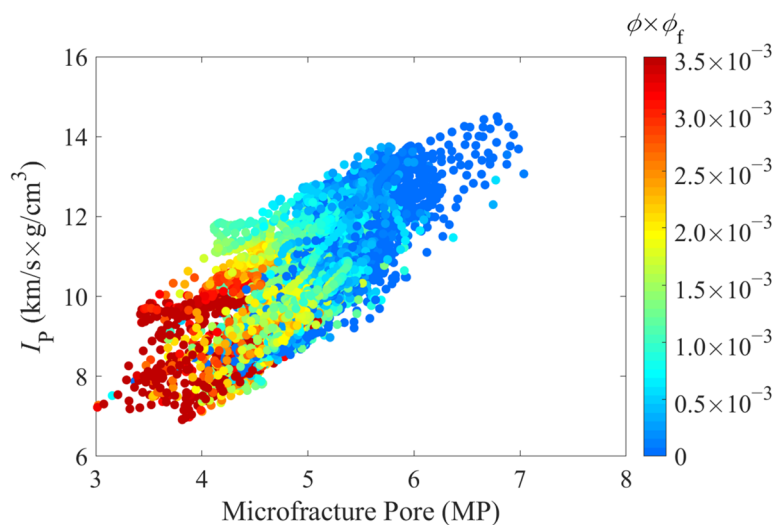
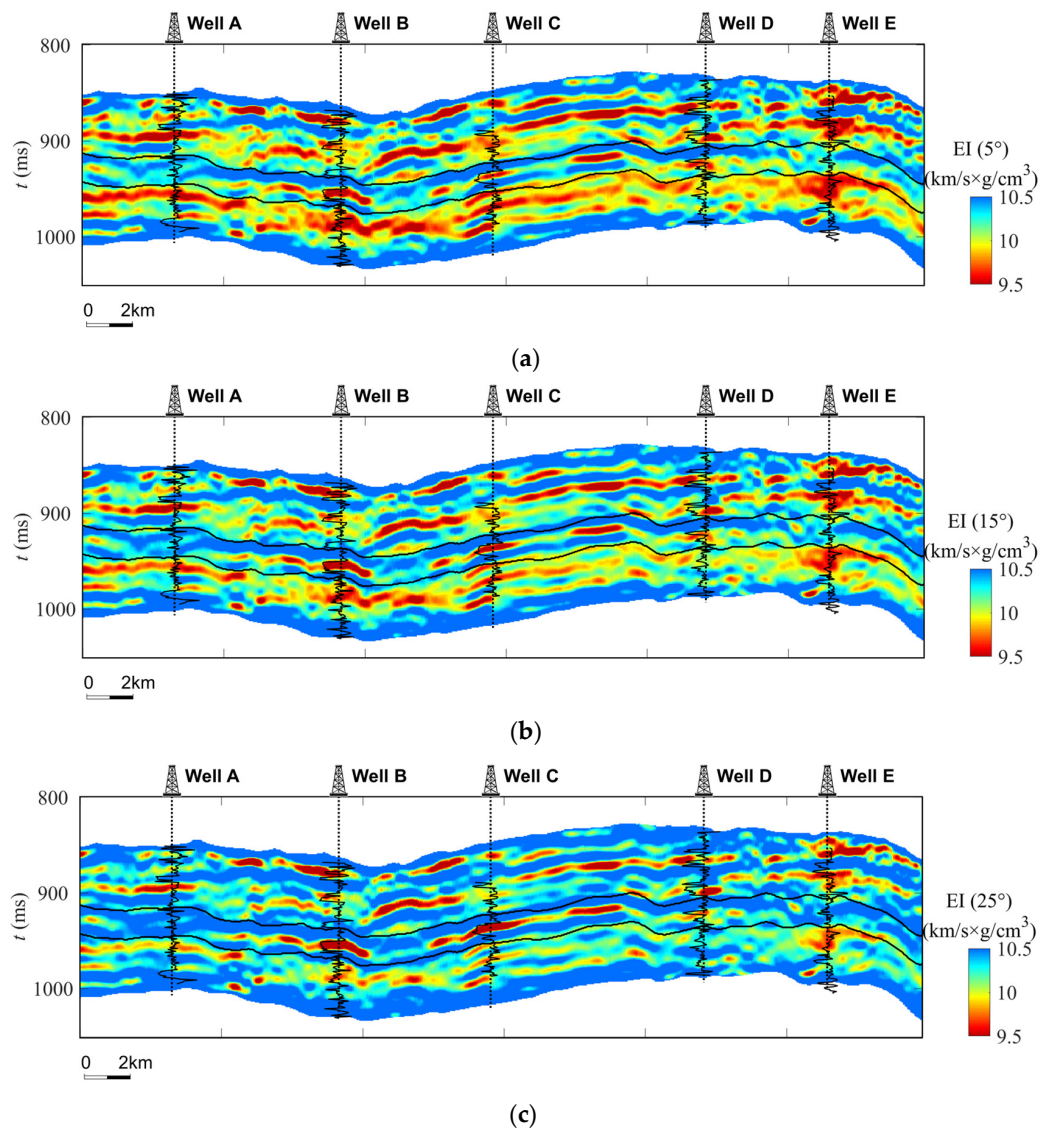**Figure 10.** Cross-plot of I_P versus MP($\theta_{\mathrm{max2}} = 45°$), as color-coded by $\phi \times \phi_f$.

Figure 11. Profiles of the elastic impedances (**a**) EI(5°), (**b**) EI(15°), and (**c**) EI(25°) across the A, B, C, D, and E wells, with overlapping GR loggings for the wellbores.
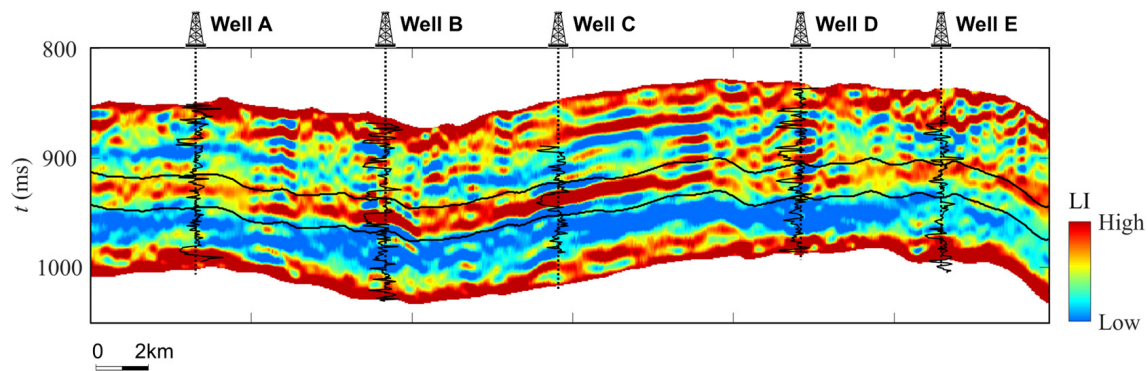
Figure 12. Profile of LI across the A, B, C, D, and E wells, with overlapping GR loggings for the wellbores.

Calculated MP profiles are, together with overlapping permeability loggings, displayed in Figure 13. As discussed above, the MP parameter could be used to estimate $\phi \times \phi_f$ in the evaluation of the development of total porosity and microfracture porosity. As can be seen in Figure 13, the low-value anomalies of the MP parameter showed a good agreement with the high permeability that was measured in gas wells B, C, and D. However, the tight formations in gas well A showed a very low permeability and no anomalies in the MP parameter. In addition, the weak MP anomalies in the dry well E corresponded to sparsely distributed permeability. Therefore, the results presented in Figure 13 have proven the applicability of the MP parameter in the determination of permeable areas of the tight formations in the studied area.
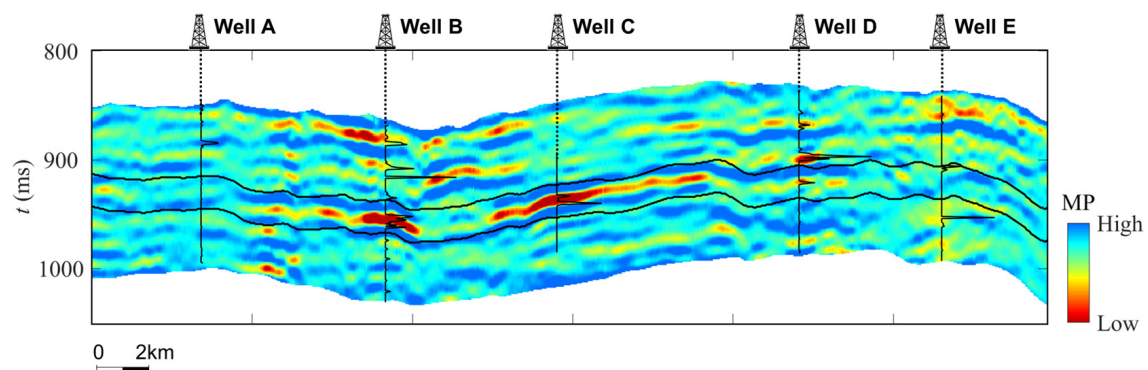

Figure 13. Profile of MP across the A, B, C, D, and E wells, with overlapping permeability loggings for the wellbores.

Furthermore, the obtained three-dimensional (3D) data of LI and MP are presented in Figures 14 and 15, respectively. They provided useful information for the identification of tight sandstones and potential permeable zones in the studied area.

3.5. Comprehensive Characterization of the Tight Gas Sandstone Reservoir

Comprehensive characterization of tight sandstones should consider both optimal lithologies indicated by LI and permeable zones suggested by MP. In addition, the bulk modulus (K) or compressibility ($1/K$) were suggested for characterizing gas-bearing tight sandstones because these properties were considered to be related to the effects of gas saturation in the tight sandstones in the studied area [6,36]. Lower K, or higher $1/K$, was regarded to indicate higher gas saturation in the tight sandstones. Figure 16 shows the section of K computed from the results of seismic elastic inversion.
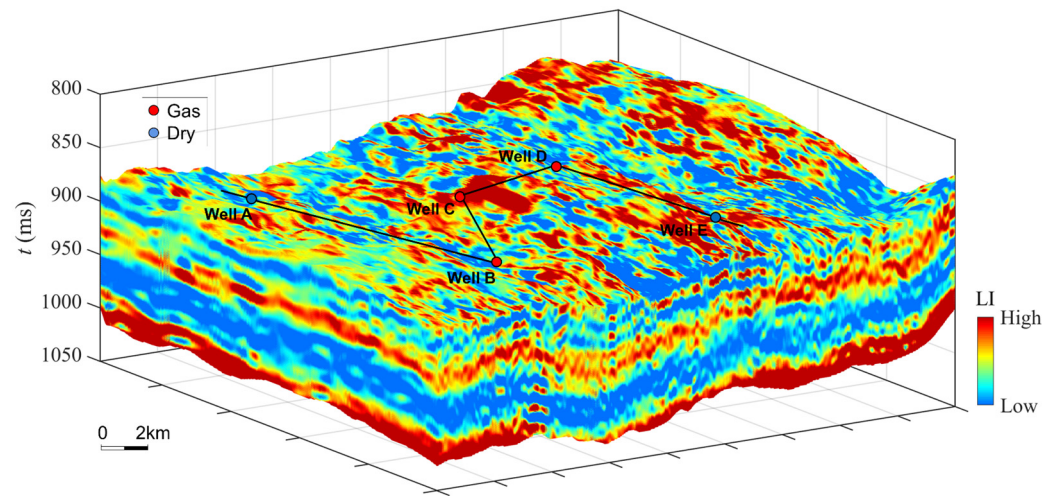
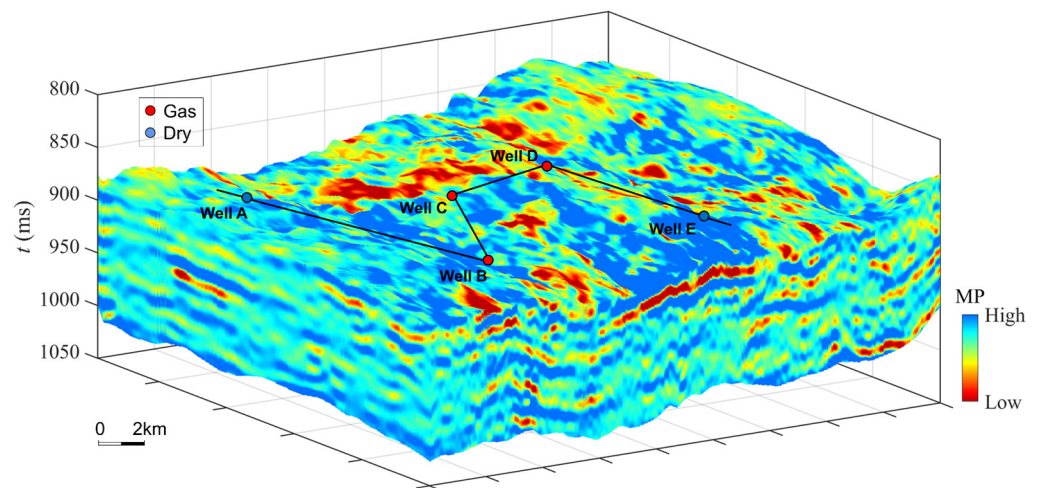**Figure 14.** The calculated 3D data of LI in the studied region.

Figure 15. The calculated 3D data of MP in the studied region.
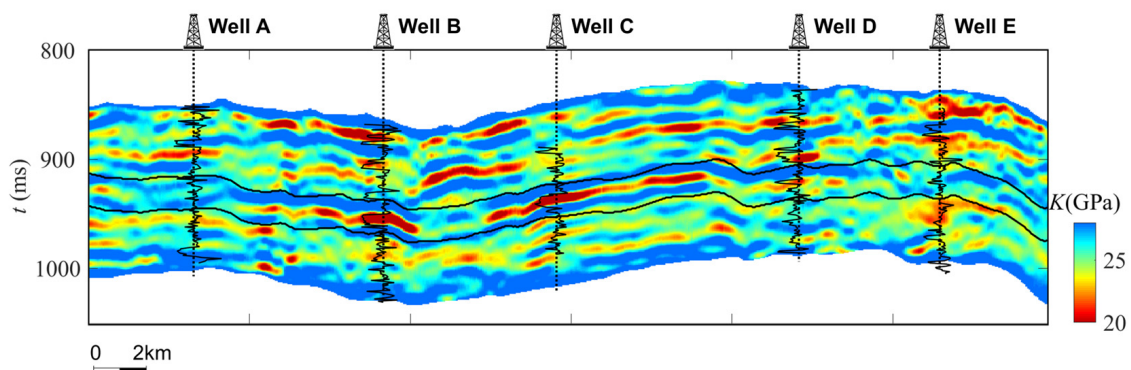
Figure 16. Profile of *K* across the A, B, C, D, and E wells, with overlapping GR loggings for the wellbores.

Then, a combination factor (*F*) was proposed to comprehensively consider the effects of lithology, pore space, and gas saturation:

$$F = \text{Normalized}(\text{LI}) \times \text{Normalized}\left(\frac{1}{\text{MP}}\right) \times \text{Normalized}\left(\frac{1}{K}\right) \qquad (23)$$

where the involved properties were normalized.

Figure 17 shows the *F* profile, where the overlapping GR logging curves indicate tight sandstones in the boreholes. Also, Figure 18 presents the calculated 3D data of *K* for the tight formations in the studied region. Furthermore, Figure 19 shows the calculated 3D data of *F* that has been computed from the results presented in Figures 14, 15 and 18. As discussed above, the obtained factor, *F*, reflects the combined effects of lithology, pore space, and gas saturation and can, therefore, be used for a comprehensive characterization of tight sandstones in the studied area.

Figure 17. Profile of *F* across the A, B, C, D, and E wells, with overlapping GR loggings for the wellbores.

Figure 18. The calculated 3D data of *K* in the studied region.

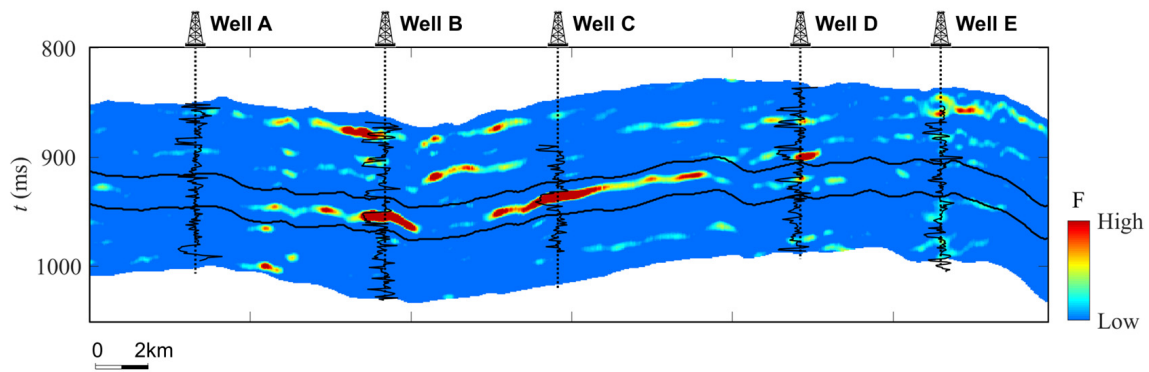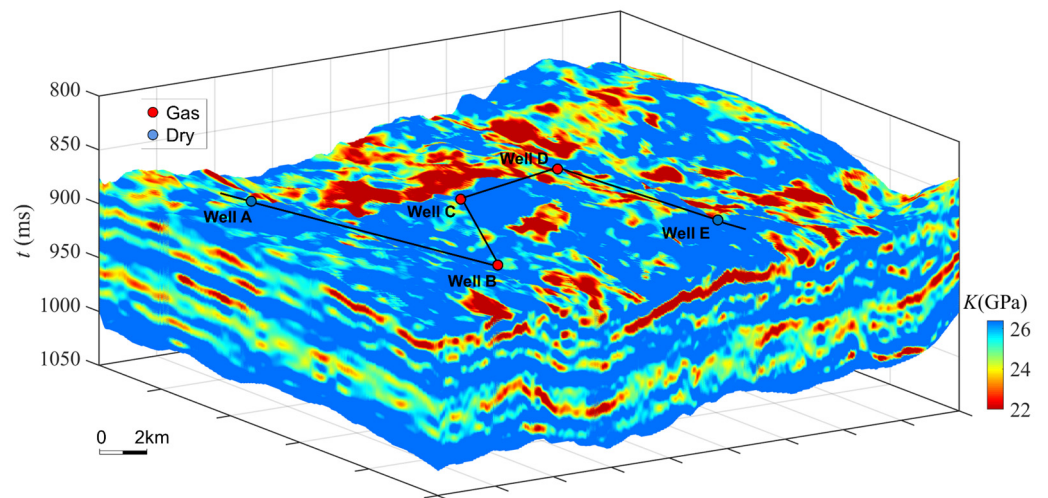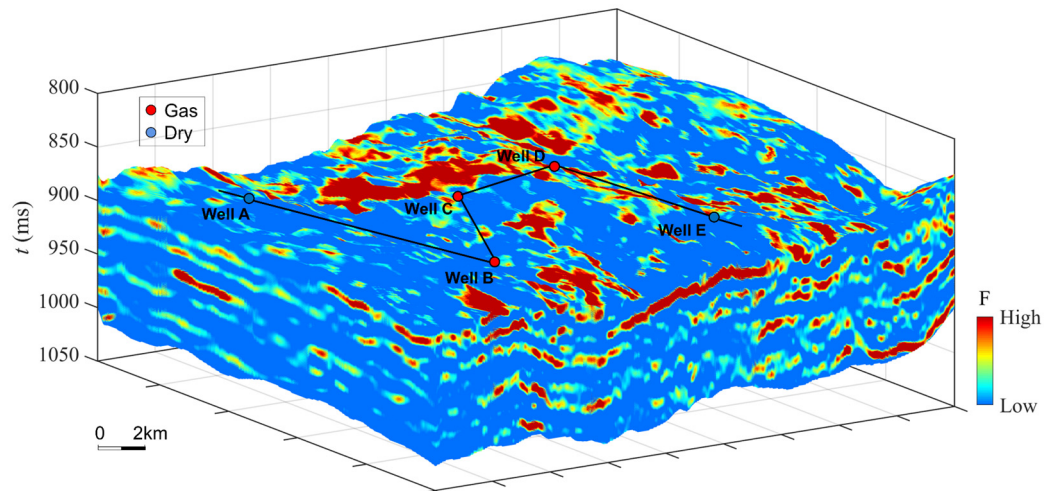**Figure 19.** The calculated 3D data of *F* in the studied region.

4. Discussion

Successful exploration and development of tight gas sandstones require identifying premium lithology and predicting pore structures, which are two controlling factors of high-quality reservoirs. However, direct estimation of these parameters using seismic methods is challenging owing to the complex rock physical characteristics of tight sandstones [37–40]. In the present study, we have focused on the direct estimation of the lithology and pore structure in tight formations and proposed an indicator of high-quality tight sandstone gas reservoirs, comprehensively considering the effects of lithology, pore structure, and gas saturation. Accordingly, a seismic inversion method based on rock physical modeling was proposed where the primary objective of the proposed method was to incorporate the rock physical constraints in the seismic inversion. Appropriate rock physical modeling methods were used to derive useful information from well-log data to provide such constraints. Despite many sophisticated models for the poroelastic behaviors of rocks [16,17], the DP model [14,15] has been validated as a practical modeling tool for tight sandstones. The microfracture porosity, ϕ_f, was then regarded as an essential parameter in the modeling using logging data (Figure 6). In addition, the obtained ϕ_f could be further used to estimate the microfracture development.

As compared by using only GR values, the proposed $GR/V_P{}^2$ factor, as represented by the lithology indicator (LI), showed an improved performance in the discrimination of tight sandstones from mudstones (Figure 7). In addition, the proposed $\phi \times \phi_f$ factor, as represented by the pore structure parameter (MP), provided a straightforward estimation of the total and microfractural porosity. Thus, the MP parameter could be used as an indicator of permeable areas in tight formations. Moreover, the proposed indicators LI and MP could be determined from the I_P and I_S values by using Equations (2) and (3) and the optimized rotation angles (Figure 8). The results presented in Figures 9 and 10 show the effectiveness of the LI and MP indicators, respectively, in the semi-quantitative predictions of the lithology and permeable zones.

The obtained LI and MP parameters provided the basis for the establishment of a new AVO equation. By using I_P and I_S according to Equations (2) and (3), although the direct quantitative interpretation of LI and MP was a straightforward alternative, it was suggested that a direct pre-stack inversion of the reservoir parameters could reduce the cumulative errors [27]. The proposed AVO equation was, therefore, further extended to the form of an elastic impedance to facilitate direct estimations of the lithology and pore structure.

As illustrated in Figures 12 and 13, the application results suggested that the seismic-inverted LI and MP parameters could be used as effective indicators of the optimal lithology and permeable zones of tight formations in the studied region. The estimated LI and MP values agreed with the reservoir properties that were measured in the wellbores and were consistent with the production status of the wells. In addition, among the five boreholes in the studied area, only the logging data from the A, B, and C wells were used in the performance of the rock physical modeling and analyses (Figures 7 and 8). Therefore, the A, B, and C wells could be regarded as constrained wells, while the D and E wells were regarded as test wells. As can be seen in Figures 12 and 13, the seismic-inverted results showed a good agreement for all five wells, which further proved the applicability of the proposed methods for the characterization of tight sandstones in the studied region.

5. Conclusions

Based on rock physical modeling, a seismic inversion method for direct prediction of the optimal lithology and pore structure in tight formations has been developed in the present study. The following conclusions could be drawn from the obtained results:

(1)　The DP model was validated as a useful modeling tool for tight sandstones with complex pore structures. The microfracture porosity, ϕ_f, could be used as a practical fitting parameter when modeling the velocities of the tight sandstones and acts as a useful factor in the evaluation of microfracture development;

(2) By using the framework of the Poisson impedance, the proposed lithology indicator, LI, and the pore structure parameter, MP, were obtained from the maximum correlation between GR/V_P^2, $\phi \times \phi_f$, and the elastic properties I_P and I_S. The LI indicator showed satisfactory performance in the discrimination of tight sandstones from mudstones. The MP indicator provided an applicable indicator for the permeable zones in tight formations;

(3) A new AVO equation was established based on the optimized LI and MP parameters. Real data applications showed that the seismic-inverted LI and MP parameters could function as useful indicators for the optimal lithology and permeable zones in the tight gas sandstones in Ordos Basin, China. The obtained results were consistent with the measured petrophysical properties in the wellbores and agreed with the production status of the wells. Furthermore, a combined F, considering the comprehensive effects of lithology, pore structure, and gas saturation, provided a useful method for the identification of favorable areas in tight formations.

With the advancement of experiments and rock physics modeling methods, the framework proposed in the present study may help in the development of other direct inversions of reservoir properties for various hydrocarbon resources.

Author Contributions: Conceptualization, Z.G.; methodology, Z.G.; software, H.J.; validation, Z.G. and H.J.; formal analysis, Z.G.; investigation, Z.G., H.J. and C.L.; resources, C.L.; data curation, H.J.; writing—original draft preparation, Z.G. and H.J.; writing—review and editing, Z.G.; visualization, H.J.; project administration, Z.G.; funding acquisition, Z.G. All authors have read and agreed to the published version of the manuscript.

Data Availability Statement: Data are contained within the article.

Appendix A

Hashin and Shtrikman [32] proposed a method to estimate the high and low elastic bounds of the elastic modulus $K^{HS\pm}$ and $\mu^{HS\pm}$:

$$K^{HS\pm} = K_1 + \frac{f_2}{(K_2 - K_1)^{-1} + f_1\left(K_1 + \frac{4}{3}\mu_1\right)^{-1}}, \tag{A1}$$

$$\mu^{HS\pm} = \mu_1 + \frac{f_2}{(\mu_2 - \mu_1)^{-1} + \frac{2f_1(K_1 + 2\mu_1)}{5\mu_1\left(K_1 + \frac{4}{3}\mu_1\right)}}, \tag{A2}$$

where K_i and μ_i are the bulk and shear modulus, respectively, and f_i is the volumetric fraction of the corresponding components in rocks (with i = 1, 2). The elastic moduli of the solid matrix can be estimated by the average of the upper and lower bounds in Equations (A1) and (A2).

The more general forms of the bounds are shown in Equations (A3) and (A4), which can be used for more than two constitutions:

$$K^{HS+} = \Lambda(\mu_{\max}), K^{HS-} = \Lambda(\mu_{\min}) \tag{A3}$$

$$\mu^{HS+} = \Gamma\left[\zeta(K_{\max}, \mu_{\max})\right], \mu^{HS-} = \Gamma[\zeta(K_{\min}, \mu_{\min})] \tag{A4}$$

where

$$\Lambda(z) = \left\langle \frac{1}{K(r) + \frac{4}{3}z} \right\rangle - \frac{4}{3}z \tag{A5}$$

$$\Gamma(z) = \left\langle \frac{1}{\mu(r) + z} \right\rangle^{-1} - z \tag{A6}$$

$$\zeta(K, \mu) = \frac{\mu}{6} \left(\frac{9K + 8\mu}{K + 2\mu} \right) \tag{A7}$$

The parentheses, $<\cdot>$, in Equations (A5) and (A6) express the averages of the material. That is, each constitution is weighted equally according to its volume content.

Berryman [33] proposed a method to estimate the equivalent elastic moduli by using the self-consistent approximation (SCA) method, as expressed by Equations (A8) and (A9):

$$\sum_{i=1}^{n} x_i (K_i - K_{SC}^*) P^{*i} = 0, \tag{A8}$$

$$\sum_{i=1}^{n} x_i (\mu_i - \mu_{SC}^*) Q^{*i} = 0, \tag{A9}$$

where i represents the i-th phase and x_i corresponds to its volume fraction. Also, K_i and μ_i are the bulk and shear modulus, respectively, of the i-th constituent. P^{*i} and Q^{*i}, respectively, are the corresponding geometrical factors.

In the present study, the fluids have been assumed to have a homogeneous distribution. The modulus of the mixed fluid was expressed as shown in Equation (A10) [41]:

$$K_f = S_w K_w + S_g K_g, \tag{A10}$$

where S_w and S_g are the water and gas saturation, respectively. Also, K_w and K_g are the bulk moduli of the water and gas, respectively.

Furthermore, the density of the fluid mixture was estimated by using Equation (A11):

$$\rho_f = S_w \rho_w + S_g \rho_g, \tag{A11}$$

where ρ_w and ρ_g are the water and gas densities, respectively.

References

1. Yang, H.; Liu, X.S.; Yang, Y. Status and prospects of tight gas exploration and development in the Ordos Basin. *Strateg. Study CAE* **2012**, *14*, 40–48. [CrossRef]
2. Hu, C.Y.; Qian, K.; Wang, X.Q.; Shi, Z.S.; Zhang, G.W.; Xu, H.Z. Critical factors for the formation of an Upper Paleozoic giant gas field with multiple gas reservoirs in Ordos Basin and the transmutation of gas reservoir properties. *Acta Petrol. Sin.* **2010**, *31*, 879–884. [CrossRef]
3. Li, X.Z.; Zhang, M.L.; Xie, W.R. Controlling factors for lithologic gas reservoir and regularity of gas distribution in the Upper Paleozoic of Ordos Basin. *Acta Petrol. Sin.* **2009**, *30*, 168–175. [CrossRef]
4. Wang, D.X. A study on the rock physics model of gas reservoir in tight sandstone. *Chin. J. Geophys.* **2017**, *60*, 64–83. [CrossRef]
5. Yin, H.; Zhao, J.; Tand, G.; Zhao, L.; Ma, X.; Wang, S. Pressure and fluid effect on frequency-dependent elastic moduli in fully saturated tight sandstone. *Geophys. Res. Solid Earth* **2017**, *122*, 8925–8942. [CrossRef]
6. Guo, Z.Q.; Zhao, D.Y.; Liu, C. Gas prediction using an improved seismic dispersion attribute inversion for tight sandstone gas reservoirs in the Ordos Basin, China. *J. Nat. Gas Sci. Eng.* **2022**, *101*, 104499. [CrossRef]
7. Guo, Z.Q.; Zhao, D.Y.; Liu, C. A New Seismic Inversion Scheme Using Fluid Dispersion Attribute for Direct Gas Identification in Tight Sandstone Reservoirs. *Remote Sens.* **2022**, *14*, 5326. [CrossRef]
8. Zhang, J.; Li, X.Z.; Shen, W.J.; Gao, S.S.; Liu, H.X.; Ye, L.Y.; Fang, F.F. Study of the Effect of Movable Water Saturation on Gas Production in Tight Sandstone Gas Reservoirs. *Energies* **2020**, *13*, 4645. [CrossRef]
9. Pan, X.P.; Zhang, G.Z. Amplitude variation with incident angle and azimuth inversion for Young's impedance, Poisson's ratio and fracture weaknesses in shale gas reservoirs. *Geophys. Prosp.* **2019**, *67*, 1898–1911. [CrossRef]
10. Pan, X.P.; Zhang, P.F.; Zhang, G.Z.; Guo, Z.W.; Liu, J.X. Seismic characterization of fractured reservoirs with elastic impedance difference versus angle and azimuth: A low-frequency poroelasticity perspective. *Geophysics* **2021**, *86*, M123–M139. [CrossRef]
11. Zhang, G.Z.; Yang, R.; Zhou, Y.; Li, L.; Du, B.Y. Seismic fracture characterization in tight sand reservoirs: A case study of the Xujiahe Formation, Sichuan Basin, China. *Appl. Geophys.* **2022**, *203*, 104690. [CrossRef]
12. Guo, Z.Q.; Nie, N.F.; Liu, C. Fracture characterization based on improved seismic amplitude variation with azimuth inversion in tight gas sandstones, Ordos Basin, China. *Mar. Pet. Geol.* **2022**, *146*, 105941. [CrossRef]

13. Liu, Y.S.; Zhu, Z.P.; Pan, R.F.; Gao, B.; Jin, J. Analysis of AVAZ Seismic Forward Modeling of Fracture-Cavity Reservoirs of the Dengying Formation, Central Sichuan Basin. *Energies* **2022**, *15*, 5022. [CrossRef]

14. Smith, T.M.; Sayers, C.M.; Sondergeld, C.H. Rock properties in low-porosity/low-permeability sandstones. *Lead. Edge* **2009**, *28*, 48–59. [CrossRef]

15. Ruiz, F.; Cheng, A. A rock physics model for tight gas sand. *Lead. Edge* **2010**, *29*, 1484–1489. [CrossRef]

16. Sun, W.; Ba, J.; Carcione, J.M. Theory of wave propagation in partially saturated double-porosity rocks: A triple-layer patchy model. *Geophys. J. Int.* **2016**, *205*, 22–37. [CrossRef]

17. Ba, J.; Xu, W.; Fu, L.; Carcione, J.M.; Zhang, L. Rock anelasticity due to patchy saturation and fabric heterogeneity: A double double-porosity model of wave propagation. *Geophys. Res. Solid Earth* **2017**, *122*, 1949–1976. [CrossRef]

18. Guo, Z.Q.; Qin, X.Y.; Zhang, Y.M.; Niu, C.; Wang, D.; Ling, Y. Numerical investigation of the effect of heterogeneous pore structures on elastic properties of tight gas sandstones. *Front. Earth Sci.* **2021**, *9*, 641637. [CrossRef]

19. Cheng, W.; Ba, J.; Carcione, J.M.; Pang, M.Q.; Wu, C.F. Estimation of the Pore Microstructure of Tight-Gas Sandstone Reservoirs with Seismic Data. *Front. Earth Sci.* **2021**, *9*, 646372. [CrossRef]

20. Ruan, C.; Ba, J.; Carcione, J.M.; Chen, T.; He, R. Microcrack Porosity Estimation Based on Rock Physics Templates A Case Study in Sichuan Basin, China. *Energies* **2021**, *14*, 7225. [CrossRef]

21. Zhou, H.T.; Li, D.Y.; Liu, X.T.; Du, Y.S.; Gong, W. Sweet spot prediction in tight sandstone reservoir based on well-bore rock physical simulation. *Pet. Sci.* **2019**, *16*, 1285–1300. [CrossRef]

22. Tan, W.H.; Ba, J.; Müller, T.; Fang, G.; Zhao, H.B. Rock Physics Model of Tight Oil Siltstone for seismic prediction of brittleness. *J. Geophys. Prosp.* **2020**, *68*, 1554–1574. [CrossRef]

23. Zhang, T.T.; Sun, Y.F. Two-parameter prestack seismic inversion of porosity and pore-structure parameter of fractured carbonate reservoirs: Part 1—Methods. *Interpretation* **2018**, *6*, SM1–SM8. [CrossRef]

24. Zhang, T.T.; Zhang, R.F.; Tia, J.Z.; Lu, L.F.; Qin, F.Q.; Zhao, X.Z.; Sun, Y.F. Two-parameter prestack seismic inversion of porosity and pore-structure parameter of fractured carbonate reservoirs: Part 2—Applications. *Interpretation* **2018**, *6*, SM9–SM17. [CrossRef]

25. Wei, Y.L.; Zhao, L.Y.; Liu, W.; Zhang, X.; Guo, Z.J.; Wu, Z.L.; Yuan, S.H. Coalbed Methane Reservoir Parameter Prediction and Sweet-Spot Comprehensive Evaluation Based on 3D Seismic Exploration: A Case Study in Western Guizhou Province, China. *Energies* **2022**, *16*, 367. [CrossRef]

26. Aleardi, M. Estimating petrophysical reservoir properties through extended elastic impedance inversion: Applications to off-shore and on-shore reflection seismic data. *J. Geophy. Eng.* **2018**, *15*, 2079–2090. [CrossRef]

27. Zhang, F.C.; Yang, J.Y.; Li, C.H.; Li, D.; Gao, Y. Direct inversion for reservoir parameters from prestack seismic data. *J. Geophy. Eng.* **2020**, *17*, 993–1004. [CrossRef]

28. Guo, Z.Q.; Qin, X.Y.; Liu, C. Pore and microfracture characterization in tight gas sandstone reservoirs with a new rock-physics-based seismic attribute. *Remote Sens.* **2023**, *15*, 289. [CrossRef]

29. Li, X.Y.; Wang, J.C.; Zhao, D.D.; Ni, J.; Lin, Y.P.; Zhang, A.G.; Zhao, L.; Liu, Y.M. Quantitative Evaluation of Water-Flooded Zone in a Sandstone Reservoir with Complex Porosity-Permeability Relationship Based on J-Function Classification: A Case Study of Kalamkas Oilfield. *Energies* **2022**, *15*, 7037. [CrossRef]

30. Hashin, Z.; Shtrikman, S. A variational approach to the theory of the elastic behaviour of multiphase materials. *Mech. Phys. Solids* **1963**, *11*, 127–140. [CrossRef]

31. Berryman, J.G. Long-wavelength propagation in composite elastic media II. Ellipsoidal inclusions. *J. Acoust. Soc. Am.* **1980**, *68*, 1820–1831. [CrossRef]

32. Quakenbush, M.; Shang, B.; Tuttle, C. Poisson impedance. *Lead. Edge* **2006**, *25*, 128–138. [CrossRef]

33. Fatti, J.L.; Smith, G.C.; Vail, P.J.; Strauss, P.J.; Levitt, P.R. Detection of gas in sandstone reservoirs using AVO analysis: A 3-D seismic case history using the Geostack technique. *Geophysics* **1994**, *59*, 1362–1376. [CrossRef]

34. Connolly, P. Elastic impedance. *Lead. Edge* **1999**, *18*, 438–452. [CrossRef]

35. Whitcombe, D.N. Elastic impedance normalization. *Geophysics* **2002**, *67*, 60–62. [CrossRef]

36. Yang, H.; Wang, D.; Zhang, M.; Wang, Y.; Liu, L.; Zhang, M. Seismic prediction method of pore fluid in tight gas reservoirs, Ordos Basin, NW China. *Pet. Explor. Dev.* **2017**, *44*, 544–551. [CrossRef]

37. Fan, X.; Zhang, G.; Zhang, J. Prediction method of pore structure parameters oftight sandstone. In *SEG Technical Program Expanded Abstracts 2019*; Society of Exploration Geophysicists: Houston, TX, USA, 2019.

38. Li, H.B.; Zhang, J.J.; Pan, H.J.; Gao, Q. Nonlinear simultaneous inversion of porestructure and physical parameters based on elastic impedance. *Sci. China Earth Sci.* **2021**, *64*, 977–991. [CrossRef]

39. Cui, H.; Zhong, N.; Li, J.; Wang, D.; Li, Z.; Hao, A.; Liang, F. Study on the lower limits of petrophysical parameters of the Upper Paleozoic tight sandstone gas reservoirs in the Ordos Basin, China. *J. Nat. Gas Geosci.* **2017**, *2*, 21–28. [CrossRef]

40. Ren, J.; Zhang, L.; Ezekiel, J.; Ren, S.; Meng, S. Reservoir characteristics and productivity analysis of tight sand gas in Upper Paleozoic Ordos Basin China. *J. Nat. Gas Sci. Eng.* **2014**, *19*, 244–250. [CrossRef]

41. Domenico, S.N. Elastic properties of unconsolidated porous sand reservoirs. *Geophysics* **1977**, *42*, 1339–1368. [CrossRef]